

Layer-by-Layer Epitaxy of Multilayer MoS₂ Wafers

Qinqin Wang^{1,2†}, Jian Tang^{1,2†}, Xiaomei Li^{1,2}, Jinpeng Tian^{1,2}, Jing Liang⁴, Na Li^{1,3}, Depeng Ji³, Lede Xian³, Yutuo Guo^{1,2}, Lu Li^{1,2}, Qinghua Zhang^{1,2}, Yanbang Chu^{1,2}, Zheng Wei^{1,2}, Yanchong Zhao^{1,2}, LuoJun Du¹, Hua Yu^{1,3}, Xuedong Bai^{1,2}, Lin Gu^{1,2}, Kaihui Liu⁴, Wei Yang^{1,2}, Rong Yang^{1,2,3}, Dongxia Shi^{1,2} & Guangyu Zhang^{1,2,3*}

¹ Beijing National Laboratory for Condensed Matter Physics and Institute of Physics, Chinese Academy of Sciences, Beijing 100190, China

² School of Physical Sciences, University of Chinese Academy of Sciences, Beijing 100190, China

³ Songshan Lake Materials Laboratory, Dongguan 523808, China

⁴ Collaborative Innovation Center of Quantum Matter and School of Physics, Peking University, Beijing 100871, China

[†] Authors contribute equally to this work.

* Corresponding author. Email: gyzhang@iphy.ac.cn

Two-dimensional (2D) semiconductor of MoS₂ has great potential for advanced electronics technologies beyond silicon¹⁻⁹. So far, high-quality monolayer MoS₂ wafers¹⁰⁻¹² are already available and various demonstrations from individual transistors to integrated circuits have also been shown¹³⁻¹⁵. In addition to the monolayer, multilayers have narrower band gaps but improved carrier mobilities and current capacities over the monolayer^{5,16-18}. However, achieving high-quality multilayer MoS₂ wafers remains a challenge. Here we report the growth of high quality multilayer MoS₂ 4-inch wafers via the layer-by-layer epitaxy process. The epitaxy leads to well-defined stacking orders between adjacent epitaxial layers and offers a delicate control of layer numbers up to 6. Systematic evaluations on the atomic structures and electronic properties were carried out for achieved wafers with different layer numbers. Significant improvements on device performances were found in thicker-layer field effect transistors (FETs), as expected. For example, the average field-effect mobility (μ_{FE}) at room temperature (RT) can increase from $\sim 80 \text{ cm}^2 \cdot \text{V}^{-1} \cdot \text{s}^{-1}$ for monolayer to $\sim 110/145 \text{ cm}^2 \cdot \text{V}^{-1} \cdot \text{s}^{-1}$ for bilayer/trilayer devices. The highest RT $\mu_{FE}=234.7 \text{ cm}^2 \cdot \text{V}^{-1} \cdot \text{s}^{-1}$ and a record-high on-current densities of $1.704 \text{ mA} \cdot \mu\text{m}^{-1}$ at $V_{ds}=2 \text{ V}$ were also achieved in trilayer MoS₂ FETs with a high on/off ratio exceeding 10^7 . Our work hence moves a step closer to practical applications of 2D MoS₂ in electronics.

Since the successful exfoliation of 2D MoS₂¹⁹, these ultrathin semiconductors have attracted great attentions in the field of electronics^{4,10,13-15,20}. Tremendous efforts have been devoted to exploring their scaled-up potentials, including both wafer-scale synthesis of high-quality materials and application of them in large-area devices, with a specific focus on the monolayer MoS₂ (ML-MoS₂)^{10,11,20-23}. Up to now, high-quality ML-MoS₂ wafers are already available from various growth approaches including chemical vapor deposition (CVD)^{11,12} and metal organic CVD (MOCVD)¹⁰. Depending on the growth approaches and substrates, the MOCVD/CVD ML-MoS₂ films are generally stitched from random/aligned domains with sizes featured at 1/100 micron level and have a state-of-the-art room temperature electron mobility of $\sim 30/\sim 70 \text{ cm}^2 \cdot \text{V}^{-1} \cdot \text{s}^{-1}$ in average, an electronic quality comparable with or even better than the exfoliated monolayers.

In terms of a further improvement of the electronic quality of the large-scale 2D-MoS₂, structural imperfections should be eliminated as much as possible; however, there is not much space left for monolayer MoS₂ after ten years of synthesis optimizations in this field. Another direction is to switch to multilayer MoS₂, e.g. bilayers or trilayers, since they have intrinsically higher electronic quality than monolayers^{16,18,24-27}. Indeed, with increased number of MoS₂ layers, decreased band gaps but enhanced electron mobilities and current densities have been demonstrated in exfoliated or CVD flakes^{16,27,28}. However, it currently remains a significant challenge to produce high-quality and large-scale MoS₂ multilayers with well-controlled number of layers. Previously, CVD and sulfurization have been used to produce multilayer MoS₂ in form of flakes. While those flakes are of good crystal quality, their sizes are small, typically less than $\sim 300 \mu\text{m}$ ^{25,29}. Large-scale multilayer MoS₂ films have been also synthesized, e.g. from sulfurization of precoated Mo/MoO₃ films³⁰ and atomic layer deposition (ALD)³¹. As-produced films are typically polycrystalline with the many randomly oriented domains in sizes of less than 100 nm and include co-existence of different layer thicknesses. Such poor crystalline quality, subjected to bad domain stitching and less control on the number of layers, leads to low electronic performances even worse than those achieved in MoS₂ monolayers³²⁻³⁵.

Generally, to produce MoS₂ multilayers, the best practice is to begin with monolayers, then increase their thicknesses by gradually growing additional layers. However, considering the case of free-standing MoS₂, this route is problematic in the thermodynamic point of view. The surface energy of free-standing MoS₂ increases with the number of layers^{36,37}, it is thus energetically unfavorable to increase additional layers³⁸. This fundamental thermodynamic limitation is likely to prevent large area multilayer MoS₂ with well-controlled layer numbers from being demonstrated previously. It is expected that this thermodynamic limitation might be overcome by engineering the surface energy of MoS₂ via the proximity effect.

In this work, we developed a new technique, i.e. layer-by-layer epitaxy, to grow high-quality 4-inch multilayer MoS₂ wafers with controlled number of layers. By using sapphire (0001) as the starting substrate, we successfully achieved the growth of uniform NL-MoS₂ (N=1, 2, 3), where N is the number of layers, in a layer-by-layer manner. All sapphire wafers used in our growth are 4-inch wafers cut along the zero-degree plane, or C-Cut, which were vacuum annealed at $\sim 1000 \text{ }^\circ\text{C}$ to form atomically flat surfaces before epitaxy. Note that sapphire wafers are cheap and widely used for various semiconductor thin film epitaxy; and sapphire (0001) surface is so far one of the best substrate for MoS₂ epitaxy due to a negligible lattice mismatch. Obviously, two processes are involved in this

layer-by-layer growth, i.e. heteroepitaxy of 1st layer on sapphire and homoepitaxy of (N+1)th layer on NL with N > 0, as illustrated in Figure 1a.

Both heteroepitaxy and homoepitaxy growth were performed in a multi-source oxygen-enhanced CVD system. As shown in our previous studies, this new CVD approach for monolayer MoS₂ growth features greatly enhanced growth rate and excellent film uniformity across the entire 4-inch sapphire surface (benefited from the stable and uniform S- and Mo- source supply during the growth process)¹¹. Usually, the 1st layer epitaxy on sapphire starts from nucleation at multiple sites, proceeds with the edge growth of those nuclei and eventually reaches a layer completion (i.e. full coverage on the substrate surface) via the domain-domain coalescence mechanism.

Note that monolayer MoS₂ growth on sapphire or SiO₂ substrates follows a unique self-limiting process²¹ in which additional layers can hardly be nucleated on the monolayer till its completion. After completing the 1st layer, we then increased both temperature of Mo-source (T_{Mo}) and substrate (T_{substrate}) to enable dense nucleation of the 2nd layer (see Methods). A higher T_{Mo}, in other words, a higher Mo-source flux, is found to be beneficial to achieve a higher nucleation density of the 2nd layer.

As shown above, the dedicate control of the growth kinetic process, e.g., nucleation and edge growth, is the key to achieve continuous layer epitaxy. In our growth tests, we achieved MoS₂ wafers with N up to 6. It was noticed that the ideal 2D growth mode is difficult to keep for Nth layer when N ≥ 3, leading to appearance of additional mono- or multilayer domains on NL-/MoS₂. Such failure is more and more significant with increasing N and the growth mode evolves gradually from 2D to 3D, in consistence with the classical Stranski-Krastanov growth mode⁴⁰. This layer-dependent growth mode evolution could be attributed to several reasons. Firstly, surface proximity effect reduces quickly for those thicker layers with upper surfaces farther away the sapphire surface. Besides, once the additional layers appear, their presence would amplify in the growth of subsequent layers.

Since as-grown MoS₂ films are very uniform for mono-/bilayers and quite uniform for trilayers across entire 4-inch wafers, we thus mainly focus on the bilayer and trilayer samples in the following characterizations. Fig. 1b shows typical optical images of the as-grown 4-inch mono-, bi- and trilayer MoS₂ wafers. Fig. 1c-h show typical zoom-in optic and atomic force microscope (AFM) images from these wafers, indicating the full coverage and very clean surfaces. The trilayer continuous films have certain additional small quadrilayer domains, and the coverage of them is ~30 %. The layer numbers were further confirmed by high resolution cross-section high-angle annular dark-field scanning transmission electron microscopy (HAADF-STEM) imaging (Fig. 1i-k). We can see clearly that each layer consists of one layer Mo and two layer S atoms with layer thickness of ~0.62 nm and the interface between the adjacent layers is atomically clean and sharp, reflecting the superiority of epitaxy.

In order to elucidate the layer stacking orders in these multilayer MoS₂ wafers, we further performed atomic structure characterizations by STEM. As shown in Fig. 2, there are two stacking orders in our bilayer samples, i.e. AA stacking (2L-AA, 3R phase) and AB stacking (2L-AB, 2H phase) and the corresponding atomic configurations are shown in Fig. 2a. Fig. 2b/2c show STEM images of a typical AA/AB-stacked bilayer MoS₂. Note that the AA stacked layers have no inversion symmetry while the AB stacked layers have. Fig. 2d&e also show the TEM images of a bilayer MoS₂ film with a grain

boundary. AA and AB stacked domains can be clearly distinguished and these two different stacking domains can coalesce together without any disconnect gap, revealing a crystalline continuity. Fig. 2f shows the selected-area electron diffraction (SAED) pattern at the grain boundary area, exhibiting only one set of hexagonal diffraction spots, as expected. We also characterized the trilayer samples. Different from the bilayer case, the stacking orders in trilayers are much more complicated. AAA, AAB/ABB, and ABA stacking configurations all exist, as show in Fig. 2 g-i. All these STEM images for bi- or trilayers reveal our epitaxial multilayer films having excellent lattice alignments. Benefiting from the epitaxy technique, the seamless stitching of these aligned domains leads to high crystalline quality of multilayer MoS₂ on sapphire, as will be confirmed by our latter device characterizations.

As mentioned above, MoS₂ multilayers would have N-dependent band gaps. In order to confirm it in our epitaxial samples, we thus collected optical spectra for our mono-, bi- and trilayer MoS₂ wafers. Corresponding Raman spectra are shown in Fig. 3a. In control samples of monolayer MoS₂ films, the peak frequency difference (Δ) between the E_{2g} and A_{1g} vibration modes is about ~20 cm⁻¹. As a comparison, Δ in bilayer and trilayer films are wider to a number of ~23 and ~24 cm⁻¹, respectively. Fig. 3b shows the photoluminescence (PL) spectra of our mono-, bi- and trilayer MoS₂ films. We can see a strong A-exciton peak at ~1.88 eV in the monolayer, while A- and B-exciton peaks are greatly suppressed in bi- and trilayer films due to the transition from the direct band gap to the indirect ones^{42,43}. The indirect bandgaps are of ~1.50 eV and ~1.42 eV for bilayers and trilayers, respectively, confirming the N-dependent band gaps of the multilayer MoS₂. Note that those sharp peaks at 1.79 eV are from sapphire substrates. Fig. 3c shows the optical transmittance spectra of mono-, bi-, and trilayer MoS₂ films transferred on quartz substrates and the corresponding transmittances are 94.2%, 91.6% and 84.5 % at a wavelength of ~550 nm. Due to the release of the strain after transfer, the A- and B-exciton peaks in the transmittance spectra are a little bit shifted. Using the Raman line scanning, we also investigated the wafer-scale uniformity of the as-grown mono-, bi- and trilayer MoS₂ wafers, as shown in Fig. 3 d-i. We can see these Raman peaks locate nearly the same along the entire wafer diameter, revealing a high uniformity.

Based on the obtained high-quality multilayer MoS₂ wafers, we hence fabricated FETs for performance benchmark testing. Let's look at the short channel trilayer MoS₂ FETs first. The structure of these back-gated MoS₂ FETs is illustrated in Fig. 4a. High-resolution STEM imaging at the MoS₂-Au interface (as illustrated in the bottom image of Fig. 4a) reveals a sharp contact interface without obvious damages, filamentous breaks or wrinkles^{6,44-46}. The output and transfer curves of a device with channel length (L_{ch}) of 40 nm are shown in Fig. 4 b-c. Linear output characteristics at small bias voltages (V_{ds}) suggest the ohmic contact behavior, and the source-drain currents (I_{ds}) quickly approach to saturation at small gate voltages subjected to the employment of HfO₂ ($\epsilon_r=15-20$) dielectric layer. The device features high on/off ratio of $>10^7$, sharp subthreshold swing (SS) of 200 mV/dec over 4 magnitudes, and small hysteresis of $\Delta V_g \approx 0.02$ V (at $0.1 \mu A \cdot \mu m^{-1}$). The current density (I_{ds}/W , where W is the channel width) can reach 1.70/1.22/0.94 mA· μm^{-1} at $V_{ds}=2/1/0.65$ V which is the highest ever achieved in MoS₂ transistors.

Transfer curves of mono-, bi- and trilayer devices with $L_{ch}=100$ nm are shown in Fig. 4d. We can see a significant improvement of the on-current densities while increasing the number of layers, and the corresponding I_{ds}/W of mono-, bi- and trilayer devices are 0.40, 0.64 and 0.81 mA· μm^{-1} , respectively, at $V_{ds}=1$ V and $V_g=5$ V. It was also noted that thicker MoS₂ devices show saturated currents at much

smaller V_g . In Fig. 4e, we plotted the current densities ($V_{ds}=1$ V) and on/off ratios of our devices, compared with previous data from the state-of-the-art MoS₂ devices. The good balance between high current density and high on/off ratio suggests a great potential of these epitaxial multilayer MoS₂ wafers for fabrication of integrated, high-performance and low-power electronics.

Next, we also fabricated long-channel FETs with L_{ch} varying from 5 to 50 μm and W_{ch} varying from 10 μm to 30 μm based on our multilayer MoS₂ wafers, as illustrated in the inset of Fig. 4f. Transfer curves of 150 randomly picked trilayer MoS₂ FETs with different L_{ch} and W_{ch} are shown in Fig. 4f. The overall yield of all devices is >95 %. All these devices exhibit small device-to-device variations, reflecting the uniformity of epitaxial wafers. On/off ratios, subthreshold voltages (V_{th}) and SS of these devices are also plotted in Fig. 4g. The highest on/off ratio can reach to 10^8 - 10^9 and averages at 4.5×10^8 , much higher than that achieved in the previous multilayer MoS₂ devices^{32,35,47}. V_{th} is mainly located at -1.25 ± 0.4 V and the average SS is ~ 115 mV/dec.

Finally, let's compare film conductivities of mono-, bi- and trilayer MoS₂. The sheet resistances (ρ) were extracted by transfer length method (TLM)⁴⁸ as shown in Fig. 4h. At a carrier density of $n_i \approx 4 \times 10^{13} \text{ cm}^{-2}$, ρ is 9.3, 5.4 and 3.0 $\text{k}\Omega$ for mono-, bi- and trilayer MoS₂ channels, respectively, revealing that multilayer MoS₂ is more conductive. Besides, the extracted contact resistance (R_c) is $\sim 0.61 \text{ k}\Omega \cdot \mu\text{m}$ at $n_i \approx 4 \times 10^{13} \text{ cm}^{-2}$. Although the achieved R_c is slightly larger than that of Bi-contacts reported recently⁹, Au-contacts are advantageous considering that Au is stable and widely used in the nowadays semiconductor technology. Better device performances might be achievable in future by further optimizing contact techniques. In Fig. 4i, we summarize the field effect mobilities (μ_{FE}) of these long-channel MoS₂ FETs. A significant improvement on μ_{FE} with channel layer numbers can be clearly seen, just as expected. The average μ_{FE} is ~ 80 , ~ 110 and $\sim 145 \text{ cm}^2 \cdot \text{V}^{-1} \cdot \text{s}^{-1}$ for mono-, bi- and trilayer FETs, respectively. The mobility distributions in each type of devices are fitted by Lorentz curves. The full width at the half maximum (FWHM) of the fitting is ~ 40 , ~ 50 and $\sim 60 \text{ cm}^2 \cdot \text{V}^{-1} \cdot \text{s}^{-1}$ for mono-, bi- and trilayer devices, and the increased FWHM with number of layers is partially attributed to the inhomogeneity from additional layers and need to be optimized in further studies. Remarkably, the highest μ_{FE} reaches 131.6, 217.3 and 234.7 $\text{cm}^2 \cdot \text{V}^{-1} \cdot \text{s}^{-1}$ in our mono-, bi- and trilayer devices, and all these numbers are record-high in wafer scale MoS₂ devices. Considering that, in well-developed thin film transistors (TFTs), μ_{FE} is 10-40 $\text{cm}^2 \cdot \text{V}^{-1} \cdot \text{s}^{-1}$ for indium-gallium-zinc-oxide (IGZO) TFTs and 50-100 $\text{cm}^2 \cdot \text{V}^{-1} \cdot \text{s}^{-1}$ for low-temperature polycrystalline silicon (LTPS) TFTs⁴⁹, the competitive average μ_{FE} (larger than 100 $\text{cm}^2 \cdot \text{V}^{-1} \cdot \text{s}^{-1}$) achieved in this work also reveal a great potential of these multilayer MoS₂ films for TFT applications.

As shown above, the developed layer-by-layer epitaxy on sapphire can yield uniform and large-scale multilayer MoS₂ with clean interfaces and well-controlled number of layers, e.g. 1, 2, 3. In each individual layer, the high lattice continuity/quality are accomplished via seamless stitching of large domains aligned along sapphire<11-20>. Bilayer and trilayer MoS₂ wafers exhibit remarkably improved electrical quality with respect to their monolayer counterparts, as evidenced from higher on-current densities and higher electron mobilities, suggesting a great potential of using them for 2D electronics. Regarding technological improvements, further investigations are required. Firstly, the high-temperature growth process is less compatible with the conventional semiconductor processes thus needs to be lowered. Secondly, steady improvements of wafer sizes and control of single-alignment of domains are also required for producing single-crystalline multilayers at large scale.

Besides, it is also very interesting to apply this layer-by-layer epitaxy technique for large-scale and high-quality heterogeneous 2D layers to broaden the application field of 2D semiconductors.

Methods

Layer-by-layer epitaxy of MoS₂. All growths were carried out in a home-built multi-source CVD system with three temperature zones, named zone-I, zone-II and zone-III. In a typical growth, one S-source (Alfa Aesar, 99.9%, 15 g) was loaded in zone-I and carried by Ar (40 sccm) and six MoO₃-source (Alfa Aesar, 99.999%, 30 mg each) were loaded in zone-II and carried by Ar/O₂ (40/1.7 sccm) individually. Sapphire substrates (single side polished, c-plane (0001) with off-set angle (M-axis) of 0.2±0.1 deg., 4-inch wafers) were loaded in zone-III. During the heteroepitaxy of MoS₂ on sapphire, the temperature in zone-I, zone-II, and zone-III is kept at 120 °C, 540 °C and 910 °C, respectively; while the temperature in zone-II and zone-III was increased to 570 °C and 940 °C, respectively, for homoepitaxy of MoS₂.

Structural and spectroscopic characterizations. AFM imaging was performed with Asylum Research Cypher S system. Raman and PL spectra were collected with Horiba Jobin Yvon LabRAM HR-Evolution Raman system with the excitation laser wavelength of 532 nm. SAED was performed in a TEM (JEOL Grand ARM 300 CFEG) operating at 80 kV, and atomic resolution images were achieved with an Aberration-corrected scanning transmission electron microscope Grand ARM 300 (JEOL) operating at 80 kV.

Device Fabrications and Measurements. FETs were fabricated by lithography and etching process. The device fabrication process is illustrated in Fig. S6. First, buried back-gates of Ti/Au/Ti (1/5/1 nm) were patterned on substrates by lithography and e-beam evaporation at a deposition rate of 0.01-0.05 Å/s. Second, HfO₂ with a thickness of 5-15 nm was deposited by ALD (Savannah-100 system, Cambridge NanoTech. Inc. Precursors: H₂O and tetrakis dimethylamino hafnium; Deposition temperature: 200 °C) as the gate dielectric layer. Third, MoS₂ films were etched off from sapphire substrates in KOH solution (1 Mol/L) at 110 °C and transferred onto the as-prepared HfO₂/metal-gate/sapphire surfaces. After transfer, lithography and oxygen plasma etching (Plasma Lab 80 Plus, Oxford Instruments Company) were used to define MoS₂ channel region. Finally, e-beam evaporated Au (20 nm) were deposited for source-drain contact metal. For short channel (L<100 nm) FETs, the substrate is SiO₂ and the channels were defined by standard e-beam lithography (EBL, Raith e-Line plus system) with PMMA (495 A2) as the resist layer (spin-coated at 2000-3000 rpm and baked at 180 °C for 2 min). For long channel (L>2 μm) FETs, the substrate is sapphire and the channels were defined by UV-lithography (MA6, Karl Suss) with AR-P 5350 (ALLRESIST GmbH) as positive photoresist with thickness of ~1 μm (spin-coated at 4000 rpm and baked at 100 °C for 4 min). Note that we also use oxygen plasma to clean the photoresist residues before depositing the Ti/Au/Ti back-gate electrodes before ALD. All electrical measurements were carried out in a four-probe vacuum station (base pressure ~10⁻⁶ mbar) equipped with a semiconductor parameter analyzer (Agilent B1500).

References

- 1 Liu, Y. *et al.* Promises and prospects of two-dimensional transistors. *Nature* **591**, 43-53, (2021).
- 2 Akinwande, D. *et al.* Graphene and two-dimensional materials for silicon technology. *Nature* **573**, 507-518, (2019).

- 3 Manzeli, S., Ovchinnikov, D., Pasquier, D., Yazyev, O. V. & Kis, A. 2D transition metal dichalcogenides. *Nat. Rev. Mater.* **2**, 17033, (2017).
- 4 Lin, Z. *et al.* Solution-processable 2D semiconductors for high-performance large-area electronics. *Nature* **562**, 254-258, (2018).
- 5 Mak, K. F., Lee, C., Hone, J., Shan, J. & Heinz, T. F. Atomically thin MoS₂: a new direct-gap semiconductor. *Phys. Rev. Lett.* **105**, 136805, (2010).
- 6 Wang, Y. *et al.* Van der Waals contacts between three-dimensional metals and two-dimensional semiconductors. *Nature* **568**, 70-74, (2019).
- 7 Fiori, G. *et al.* Electronics based on two-dimensional materials. *Nature Nanotechnol.* **9**, 768-779, (2014).
- 8 Desai, S. B. *et al.* MoS₂ transistors with 1-nanometer gate lengths. *Science* **354**, 99-102, (2016).
- 9 Shen, P.-C. *et al.* Ultralow contact resistance between semimetal and monolayer semiconductors. *Nature* **593**, 211-217, (2021).
- 10 Kang, K. *et al.* High-mobility three-atom-thick semiconducting films with wafer-scale homogeneity. *Nature* **520**, 656-660, (2015).
- 11 Wang, Q. *et al.* Wafer-Scale Highly Oriented Monolayer MoS₂ with Large Domain Sizes. *Nano Lett.* **20**, 7193-7199, (2020).
- 12 Li, T. *et al.* Epitaxial growth of wafer-scale molybdenum disulfide semiconductor single crystals on sapphire. *Nature Nanotechnol.* **16**, 1201-1207, (2021).
- 13 Polyushkin, D. K. *et al.* Analogue two-dimensional semiconductor electronics. *Nat. Electron.* **3**, 486-491, (2020).
- 14 Li, N. *et al.* Large-scale flexible and transparent electronics based on monolayer molybdenum disulfide field-effect transistors. *Nat. Electron.* **3**, 711-717, (2020).
- 15 Daus, A. *et al.* High-performance flexible nanoscale transistors based on transition metal dichalcogenides. *Nat. Electron.* **4**, 495-501, (2021).
- 16 Cheng, R. *et al.* Few-layer molybdenum disulfide transistors and circuits for high-speed flexible electronics. *Nat. Commun.* **5**, 5143, (2014).
- 17 Lee, G. H. *et al.* Flexible and transparent MoS₂ field-effect transistors on hexagonal boron nitride-graphene heterostructures. *ACS Nano* **7**, 7931-7936, (2013).
- 18 Li, S. L. *et al.* Thickness-dependent interfacial Coulomb scattering in atomically thin field-effect transistors. *Nano Lett.* **13**, 3546-3552, (2013).
- 19 Novoselov, K. S. *et al.* Two-dimensional atomic crystals. *Proc. Natl Acad. Sci. USA* **102**, 10451-10453, (2005).
- 20 Aljarb, A. *et al.* Ledge-directed epitaxy of continuously self-aligned single-crystalline nanoribbons of transition metal dichalcogenides. *Nat. Mater.* **19**, 1300-1306, (2020).
- 21 Yu, H. *et al.* Wafer-Scale Growth and Transfer of Highly-Oriented Monolayer MoS₂ Continuous Films. *ACS Nano* **11**, 12001-12007, (2017).
- 22 Yang, P. *et al.* Epitaxial Growth of Centimeter-Scale Single-Crystal MoS₂ Monolayer on Au(111). *ACS Nano* **14**, 5036-5045, (2020).
- 23 Yang, P. *et al.* Batch production of 6-inch uniform monolayer molybdenum disulfide catalyzed by sodium in glass. *Nat. Commun.* **9**, 979, (2018).
- 24 Xu, H. *et al.* High-Performance Wafer-Scale MoS₂ Transistors toward Practical Application. *Small* **14**, e1803465, (2018).
- 25 Zhang, X. *et al.* Transition metal dichalcogenides bilayer single crystals by reverse-flow chemical vapor epitaxy. *Nat. Commun.* **10**, 598, (2019).
- 26 Kim, S. *et al.* High-mobility and low-power thin-film transistors based on multilayer MoS₂ crystals. *Nat. Commun.* **3**, 1011, (2012).
- 27 Das, S., Chen, H. Y., Penumatcha, A. V. & Appenzeller, J. High performance multilayer MoS₂ transistors with scandium contacts. *Nano Lett.* **13**, 100-105, (2013).
- 28 Zheng, J. *et al.* High-Mobility Multilayered MoS₂ Flakes with Low Contact Resistance Grown by Chemical Vapor Deposition. *Adv. Mater.* **29**, 1604540 (2017).
- 29 Gao, Q., Zhang, Z., Xu, X., Song, J., Li, X and Wu, Y. Scalable high performance radio frequency electronics based

- on large domain bilayer MoS₂. *Nat. Commun.* **9**, 4778, (2018).
- 30 Lin, Y. C. *et al.* Wafer-scale MoS₂ thin layers prepared by MoO₃ sulfurization. *Nanoscale* **4**, 6637-6641, (2012).
 - 31 Liu, H. *et al.* Atomic layer deposited 2D MoS₂ atomic crystals: from material to circuit. *Nano Research* **13**, 1644-1650, (2020).
 - 32 Shi, Y., Li, H. & Li, L. J. Recent advances in controlled synthesis of two-dimensional transition metal dichalcogenides via vapour deposition techniques. *Chem. Soc. Rev.* **44**, 2744-2756, (2015).
 - 33 Ahn, C. *et al.* Low-Temperature Synthesis of Large-Scale Molybdenum Disulfide Thin Films Directly on a Plastic Substrate Using Plasma-Enhanced Chemical Vapor Deposition. *Adv. Mater.* **27**, 5223-5229, (2015).
 - 34 Hong, S. *et al.* Highly sensitive active pixel image sensor array driven by large-area bilayer MoS₂ transistor circuitry. *Nat. Commun.* **12**, 3559, (2021).
 - 35 Zhang, L., Dong, J. & Ding, F. Strategies, Status, and Challenges in Wafer Scale Single Crystalline Two-Dimensional Materials Synthesis. *Chem. Rev.* **121**, 6321-6372, (2021).
 - 36 Guo, Y., Wang, Z., Zhang, L., Shen, X. and Liu, F. Thickness dependence of surface energy and contact angle of water droplets on ultrathin MoS₂ films. *Phys. Chem. Chem. Phys.* **18**, 14449-14453, (2016).
 - 37 Shang, L., Lindwall, G., Wang, Y., Redwing, J. M., Anderson, T. and Liu, Z. Lateral versus vertical growth of two-dimensional layered transition-metal dichalcogenides: thermodynamic insight into MoS₂. *Nano Letters* **16**, 5742-5750, (2016).
 - 38 Bauer E. and Merwe, J. Structure and growth of crystalline superlattices: From monolayer to superlattice. *Phys. Rev. B* **33**, 3657-3671, (1986).
 - 39 Yu, H. *et al.* Precisely Aligned Monolayer MoS₂ epitaxially grown on h-BN basal plane. *Small*, **13**, 1603005, (2017).
 - 40 Stranski I N, Krastanov L. Zur Theorie der orientierten Ausscheidung von Ionenkristallen aufeinander. *Sitzungs-bericht Akademie der Wissenschaften Wien, Math.-naturwiss. Kl. Iib* **146**, 797-810, (1938).
 - 41 Shinde, S. M. *et al.* Stacking-controllable interlayer coupling and symmetric configuration of multilayered MoS₂. *NPG Asia Mater.* **10**, e468-e468, (2018).
 - 42 Chen, J. *et al.* Homoepitaxial Growth of Large-Scale Highly Organized Transition Metal Dichalcogenide Patterns. *Adv. Mater.* **30**, 1704674, (2018).
 - 43 Splendiani, A. *et al.* Emerging photoluminescence in monolayer MoS₂. *Nano Lett.* **10**, 1271-1275, (2010).
 - 44 Liu, Y. *et al.* Approaching the Schottky-Mott limit in van der Waals metal-semiconductor junctions. *Nature* **557**, 696-700, (2018).
 - 45 Allain, A., Kang, J., Banerjee, K. & Kis, A. Electrical contacts to two-dimensional semiconductors. *Nat. Mater.* **14**, 1195-1205, (2015).
 - 46 Kim, C. *et al.* Fermi Level Pinning at Electrical Metal Contacts of Monolayer Molybdenum Dichalcogenides. *ACS Nano* **11**, 1588-1596, (2017).
 - 47 Park, S. *et al.* Layer-Selective Synthesis of MoS₂ and WS₂ Structures under Ambient Conditions for Customized Electronics. *ACS Nano* **14**, 8485-8494, (2020).
 - 48 Xie, L. *et al.* Graphene-Contacted Ultrashort Channel Monolayer MoS₂ Transistors. *Adv. Mater.* **29**, 1702522, (2017).
 - 49 Myny, K. The development of flexible integrated circuits based on thin-film transistors. *Nat. Electron.* **1**, 30-39, (2018).

Acknowledgements

This work was supported by the National Key Research and Development Program, the Strategic Priority Research Program of CAS (Grant No. XDB30000000), the Key-Area Research and Development Program of Guangdong Province (Grant No. 2020B0101340001), the National Science Foundation of China (NSFC, Grant No. 11834017 & 61888102), and the Key Research Program of Frontier Sciences of CAS (Grant No. QYZDB-SSW-SLH004).

Author Contributions

G.Z. supervised this research. Q.W. performed the CVD growths and Raman characterizations. J.T. carried out device fabrications and electrical measurements with the assistance from Q.W.. X.L., Q.Z., X.B., and L.G. performed STEM characterizations. J.L., and K.L. performed SHG mapping. D.J. and L.X performed modeling and theoretical calculations. Q.W., J.T. and G.Z. wrote and all authors commented on the manuscript.

Conflict of Interest

The authors declare no conflict of interests.

Data availability

The data that support the findings of this study are available from the corresponding authors on reasonable request.

Figures and Figure captions

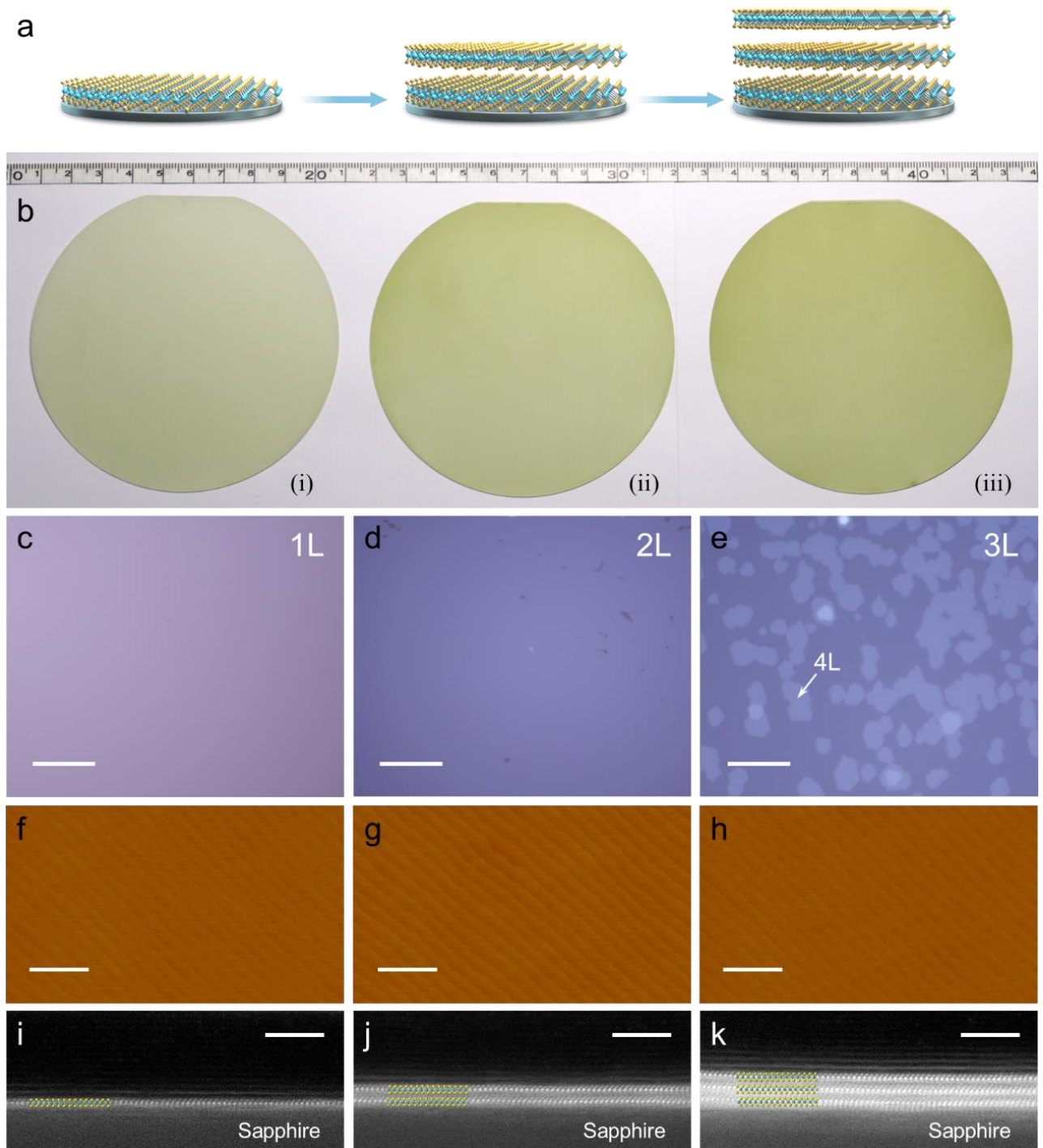


Fig. 1 | Layer-by-layer epitaxy of multilayer MoS₂ wafers. **a.** Schematic illustration of epitaxy process. **b.** Photographs of 4-inch MoS₂ wafers, (i) monolayer, (ii) bilayer, (iii) trilayer. **c-e.** Optical images of wafers shown in (b). Quadrilayer domains on the trilayer film is marked by white arrow. Scale bars, 30 μm . **f-h.** AFM amplitude images taken from mono-, bi- and trilayer wafers. Scale bars, 500 nm. **i-k.** Cross-sectional HAADF-STEM images of epitaxial mono-, bi- and trilayer MoS₂. Scale bars, 3 nm.

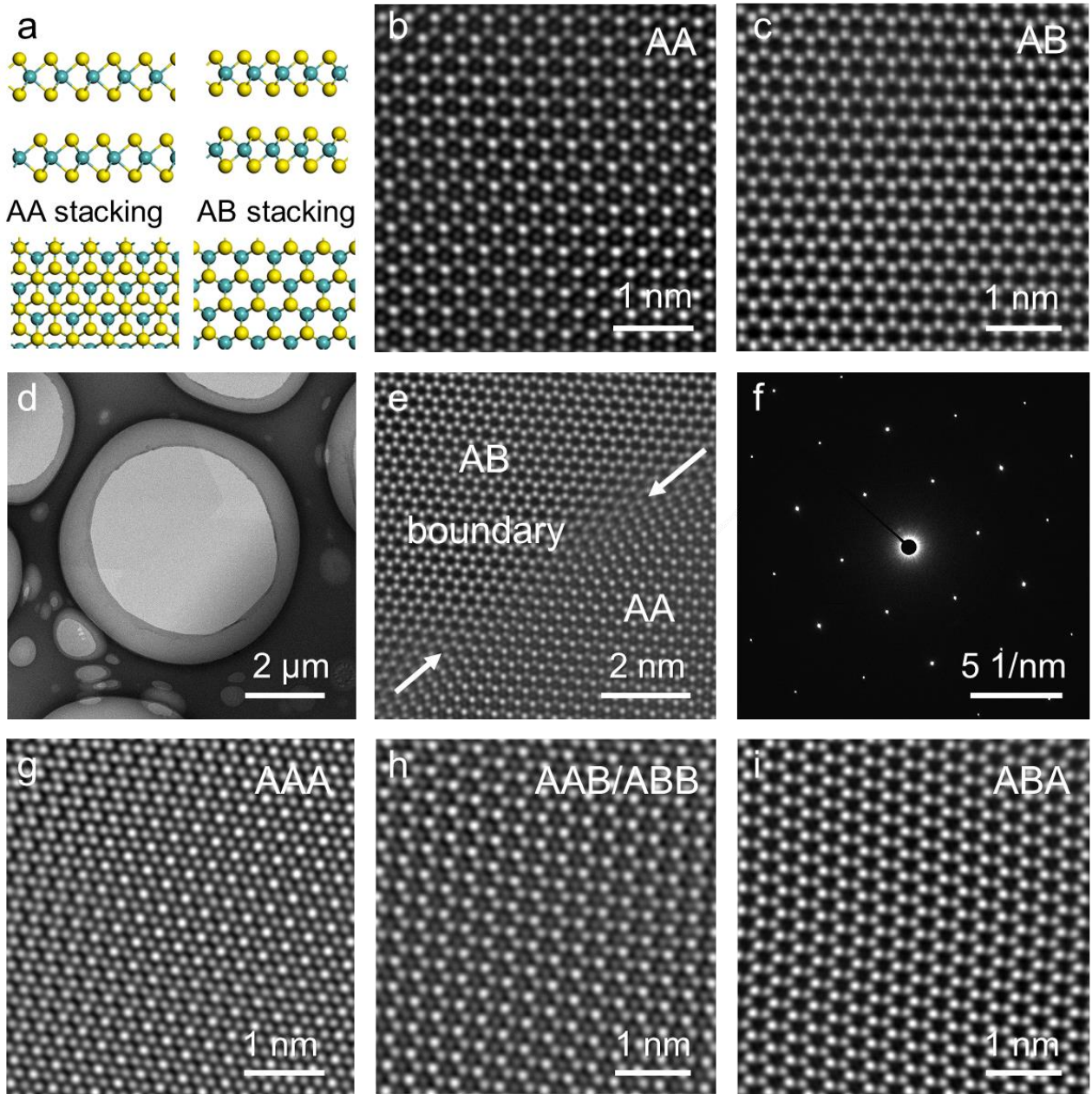


Fig. 2 | Stacking configurations in the epitaxial multilayer MoS₂. **a.** Side and top view in ball-and-stick mode of the atomic structures for AA and AB stacked MoS₂ bilayer. **b/c.** STEM images of AA/AB stacked bilayer MoS₂. **d.** STEM image of two emerged flakes with AA and AB stacking orders. **e/f.** STEM/SAED image of the boundary area shown in **d**. **g-i.** STEM images of the AAA stacked (**g**), AAB/ABB stacked (**h**) and ABA (**i**) stacked trilayer MoS₂.

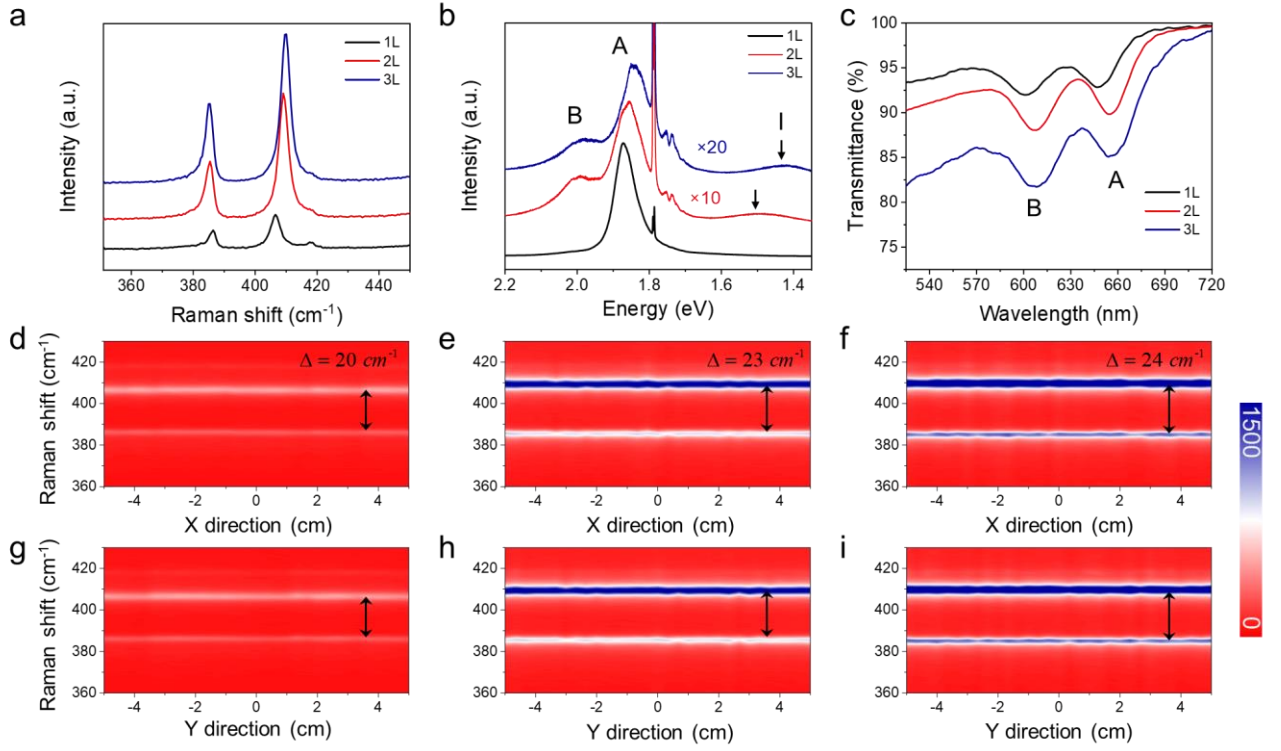


Fig. 3 | Spatial uniformity of multilayer MoS₂ wafers. **a-b.** Raman, PL, and transmittance spectra of the as-grown mono-, bi-, and trilayer MoS₂ wafers. **d-i.** Color-coded images of typical Raman line scan mapping along the horizontal and longitudinal direction of (**d, g**) monolayer, (**e, h**) bilayer and (**f, i**) trilayer MoS₂ wafers. Each line scan along either X- or Y-direction of the wafer includes 31 data points.

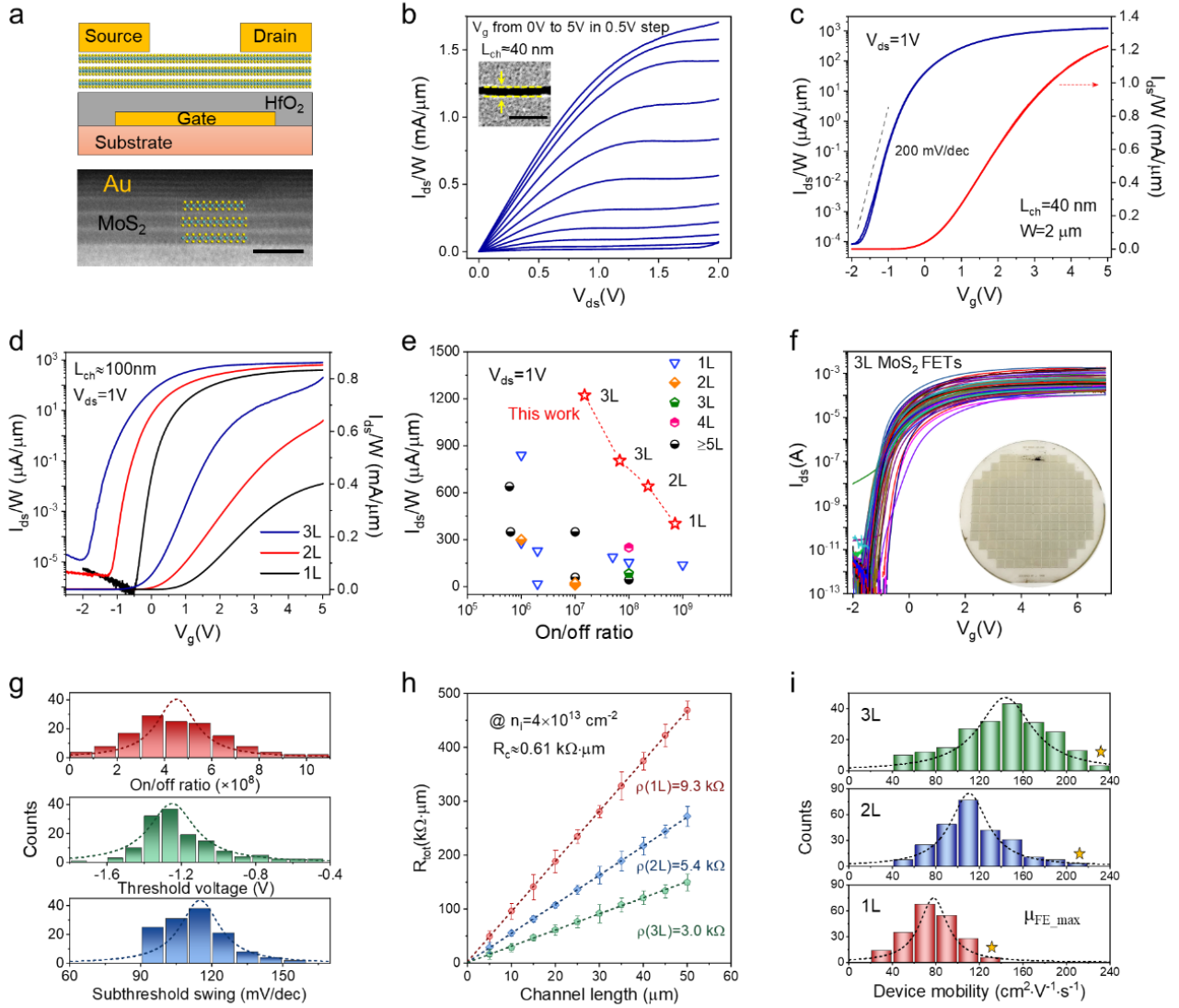


Fig. 4 | Bench-mark testing of multilayer MoS₂ FETs. **a.** Schematic view (top) of back-gated MoS₂ FET, and cross-section STEM image (bottom) of a trilayer FETs at the MoS₂-Au contact region. Scale bar, 1 nm. **b/c.** Typical output/transfer curves of a trilayer MoS₂ FET. $L_{ch}=40$ nm, $t_{HfO_2}=5$ nm. Inset to **(b)** shows the SEM image of the channel. **d.** Comparison of transfer curves of mono-, bi- and trilayer MoS₂ FETs with $L_{ch}\approx 100$ nm. **e.** The comparisons of current densities (@ $V_{ds}=1$ V) and on/off ratios with previous works. The detailed device parameters are shown in Table S1. **f.** Transfer curves of 150 trilayer MoS₂ FETs at $V_{ds}=1$ V. $L_{ch}=5-50$ μm , $t_{HfO_2}=10$ nm. Inset to **(f)** shows photograph of wafer-scale MoS₂ FET array. **g.** Statistical distribution of on/off ratio (red), threshold voltage (green) and subthreshold swing (blue) from the 150 trilayer MoS₂ FETs. **h.** The sheet resistance ρ and contact resistance R_c extracted from mono-, bi- and trilayer MoS₂ FETs. **i.** Statistical distribution of device mobility of mono-, bi- and trilayer MoS₂ FETs. The yellow stars indicate the maximum values achieved in each type of devices.